








# Macrophage-related inflammatory responses to degradation products of biodegradable molybdenum implants

Danyang Liu<sup>a,b,1</sup> , Jiahao Chen<sup>c,1</sup> , Jiannan Zhou<sup>a,b</sup> , Jingtao Dai<sup>d</sup> , Haotian Qin<sup>e</sup> , Guojiang Wan<sup>f</sup> , Junyu Qian<sup>e,\*\*\*</sup> , Ping Li<sup>a,b,\*</sup> , Jiang Li<sup>a,b,\*\*</sup> 

<sup>a</sup> School and Hospital of Stomatology, Guangdong Engineering Research Center of Oral Restoration and Reconstruction, Guangzhou Medical University, Guangzhou, 510182, PR China

<sup>b</sup> Guangzhou Key Laboratory of Basic and Applied Research of Oral Regenerative Medicine, Guangzhou, 510182, PR China

<sup>c</sup> Department of Prosthodontics, Geriatric Dentistry and Craniomandibular Disorders, Charité-Universitätsmedizin Berlin, Corporate Member of Freie Universität Berlin and Humboldt-Universität zu Berlin, Aßmannshäuser Str. 4-6, 14197, Berlin, Germany

<sup>d</sup> Department of Orthodontics, Stomatological Hospital, School of Stomatology, Southern Medical University, Guangzhou, 510515, PR China

<sup>e</sup> Department of Bone and Joint Surgery, Peking University Shenzhen Hospital, Shenzhen Peking University-The Hong Kong University of Science and Technology Medical Center, Shenzhen, 518036, PR China

<sup>f</sup> Institute of Biomedical Engineering, College of Medicine, Key Laboratory of Advanced Technologies of Materials, Ministry of Education, Southwest Jiaotong University, Chengdu, 610031, PR China

## ARTICLE INFO

### Keywords:

Molybdenum  
Biodegradable metal  
Macrophage polarization  
Biodegradability  
Immunoregulation  
Inflammatory reaction

## ABSTRACT

Metallic molybdenum (Mo) has been increasingly recognized as a potential biodegradable metal for biomedical implants. However, the macrophage-mediated inflammatory responses to Mo-based implants remain underexplored. This study examined the *in vitro* inflammatory reactions of macrophages to the degradation products of biodegradable Mo implants. The short-term and long-term biodegradation behavior and the subsequent impact on cytotoxicity, metabolism, and macrophage polarization were assessed. Both Mo and its degradation products were shown to be non-toxic within macrophage tolerance limits. Nevertheless, morphological changes and pro-inflammatory polarization were observed in cells around Mo-based specimen. Notably, matrix metalloproteinase 9 (*Mmp9*) was identified as a key gene influencing macrophage polarization in proximity to Mo. Additionally, pre-treating the Mo specimens in culture medium for 24 h significantly mitigated its stimulatory effects on cells. These results demonstrated the significance of optimizing Mo pre-treatment methods to prevent localized inflammation associated with its degradation. Specifically, pre-treatment of Mo can effectively mitigate the adverse impacts of its early degradation on macrophages and the surrounding immune environment. Our research into these early degradation phases introduces new avenues for studying molybdenum's immunomodulatory properties, potentially through precise control of its release and the targeted expression of pivotal genes.

## 1. Introduction

Biodegradable metals (BMs) are characterized by their unique ability to degrade within biological environments, combined with excellent

mechanical properties, osteoinduction capacity, and antimicrobial properties, making them promising materials for biomedical implants [1,2]. The mechanical properties of biodegradable metals have been considered as a critical parameter that defines their applications [1,3].

This article is part of a special issue entitled: Surface & Interface published in Materials Today Bio.

\* Corresponding author. School and Hospital of Stomatology, Guangdong Engineering Research Center of Oral Restoration and Reconstruction, Guangzhou Medical University, Guangzhou, 510182, PR China.

\*\* Corresponding author. School and Hospital of Stomatology, Guangdong Engineering Research Center of Oral Restoration and Reconstruction, Guangzhou Medical University, Guangzhou, 510182, PR China.

\*\*\* Corresponding author.

E-mail addresses: [junyu.qian@foxmail.com](mailto:junyu.qian@foxmail.com) (J. Qian), [pingli@gzhmu.edu.cn](mailto:pingli@gzhmu.edu.cn) (P. Li), [ljiang@gzhmu.edu.cn](mailto:ljiang@gzhmu.edu.cn) (J. Li).

<sup>1</sup> These authors contributed equally as first authors to this work.

<https://doi.org/10.1016/j.mtbio.2025.101519>

Received 12 November 2024; Received in revised form 20 January 2025; Accepted 22 January 2025

Available online 23 January 2025

2590-0064/© 2025 Published by Elsevier Ltd. This is an open access article under the CC BY-NC-ND license (<http://creativecommons.org/licenses/by-nc-nd/4.0/>).

The BMs, including magnesium (Mg) and zinc (Zn) with their acceptable mechanical properties [4,5], are primarily used as fabrication in osteosynthesis implants for stabilizing fractures, especially in cranio-maxillofacial regions [6–8]. Additionally, the degradation products can be absorbed within the body to avoid the additional surgery for the removal of implants [9,10]. To date, molybdenum (Mo) is considered as a potential biodegradable metal with the advantages of high mechanical properties (i.e., Yield Strength >350 MPa after 6 months of degradation.), beyond the counterparts of Zn and Mg [11–13]. Continuous advances in biomedical engineering and materials science have further shown that Mo holds great promise for the development of new medical devices and therapeutic solutions such as oral maxillofacial implants, cardiovascular stents and bio-battery [14,15]. Notably, Mo compounds have been shown to promote cell growth and have antimicrobial effects [16]. However, research of the application of Mo as BM implants is still in its infancy and it remains unclear whether Mo leads to adverse reactions in the human body, especially regarding macrophage-related inflammatory responses.

Macrophage is a key immune cell regulating host-material interactions [17]. Specifically, macrophage can undergo a phenotypic transition from the M0 (resting) state to the pro-inflammatory M1 (activated) state upon contact with implants, leading to the upregulation and translation of inflammation-associated genes into cytokines that provoke a widespread inflammatory response in surrounding cells [18, 19]. Previous studies demonstrated that biodegradable Zn alloys and Mg alloys can promote osseointegration through modulating macrophage phenotypes [20–22]. In turn, adverse effects of degradation products mostly cause an inflammatory response in the implanted area leading to edema, tissue damage, and implant loosening [23], and the biological response is linked to the degradation products at the implant site [24]. BM devices degrade progressively at their interface with body fluids, releasing corrosion products that elicit a host response. For example, Mg-based BMs release a suitable concentration of Mg ion during degradation and form an alkaline microenvironment that promotes the polarization of macrophages toward an anti-inflammatory phenotype [25]. The acceptable biocompatibility of Mo-based biomaterials has been observed [26–28]. Additionally, the released Mo ion can induce bone regeneration, making it a promising material for bone applications [13]. Nevertheless, recent *in vivo* studies reported that the local inflammatory reaction can be found surrounding the pure Mo-based implants, indicating that the released Mo ion might adversely affect the immune cells [29–31]. The interaction between Mo ion and immune cells remains inadequately studied. To the best of our knowledge, the influence of the degradation products of Mo-based BMs on macrophage polarization and the underlying mechanisms remain unknown [32–34].

Developing alternative bioresorbable materials are crucial for implants that guide bone tissue regeneration, as these materials must exhibit controlled corrosion behavior and produce biocompatible degradation products. Based on our prior research, Mo exhibits superior long-term corrosion resistance compared to Mg, Zn, and iron (Fe) [35]. Currently, data on the degradation behavior of Mo-based metals remain limited. The electrochemical corrosion rate of Mo in distilled water and NaCl solution ranges from 1.63 to 8.76  $\mu\text{m year}^{-1}$ , while in Hank's balanced salt solution, the corrosion rate is 6.13  $\mu\text{m year}^{-1}$  [36,37]. In phosphate-buffered saline, which simulates serum components, the corrosion rate ranges from 16 to 23  $\mu\text{m year}^{-1}$ , whereas in simulated inflammatory environments, the degradation rate of Mo can reach as high as 135–265  $\mu\text{m year}^{-1}$  [38]. A stable and uniform corrosion morphology is crucial for preventing early implant failure due to fracture [13]. However, the compatibility of soluble or insoluble by-products ( $\text{MoO}_4^{2-}$ ,  $\text{MoO}_2$  and  $\text{MoO}_3$ ) related to the degradation of Mo metal with immune cells remains unclear.

This study investigates the *in vitro* degradation behavior and cytocompatibility of biodegradable a Mo-based biodegradable metal in an immune environment, specifically examining its effects on macrophage polarization and biological function. The surface morphology and

elemental composition of Mo were characterized over a 14-day degradation period using electrochemical testing. Both direct and indirect exposure of Mo influenced the cytocompatibility, inflammation response, and M1/M2 polarization in macrophages. The potential mechanisms underlying the shift in macrophage polarization induced by degradable Mo were analyzed through RNA sequencing, with confirmatory results obtained via RT-qPCR. Thus, this study focused on i) assess the degradation behavior and composition of degradation products of Mo, ii) evaluate the effects of Mo extracts and direct contact of Mo on macrophage viability and morphology, and. iii) observe the impact of raw Mo and pre-treated Mo on the polarization and underlying cellular mechanisms of surrounding macrophages.

## 2. Materials and methods

### 2.1. Specimen preparation

Pure molybdenum (wt. 99.9 %), fabricated as described previously [39], was used in this study. The titanium alloy (Ti-6Al-4V) was set as the negative control. Ti and Mo were cut into sheets 10-mm in width, 10-mm in length, and 2-mm thick for testing. Ti and Mo were gradually polished using sandpapers of 180, 400, and 1200 grit. After polishing, the metals were immersed in 75 % ethanol and washed by ultrasonic agitation for 30 min, removed and rinsed with sterile deionized water to eliminate any residual ethanol from the surface. Before proceeding with subsequent experiments, the specimens were exposed to ultraviolet light for 30 min on each side to ensure surface sterility. The untreated pure Mo was named raw Mo (termed to R-Mo). The pre-treated pure Mo (P-Mo) was subjected to mimetic physiological degradation by pre-treatment with cell culture medium for 24 h, as previously reported [40–42].

### 2.2. *In vitro* corrosion behavior

The *in vitro* corrosion behavior of pure Mo was investigated by transient electrochemical measurement and immersion test. Briefly, potentiodynamic polarization (PDP) curves and electrochemical impedance spectra (EIS) were obtained at 37 °C utilizing an electrochemical workstation (IM6, Zahner, Germany) in Dulbecco's Modified Eagle Medium (DMEM; Thermo Scientific, CA, USA)/Ham's F-12 Nutrient Mixture (F-12; Thermo Scientific, CA, USA) cell culture medium. A three-electrode cell system, including the working electrode (research samples, exposed area ca. 0.79  $\text{cm}^2$ ), reference electrode (saturated calomel electrode, SCE), and counter electrode (platinum, 1.5 × 1.5 cm), was selected to conduct the electrochemical test. The back sides of the test samples were connected with copper wire and sealed with silicone rubber. After 15 min of stabilizing in the DMEM/F-12 medium, the PDP curves of Mo were recorded with a potential range of –1.0 to 0.2 V at a scanning rate of 1 mV/s. The self-corrosion potential ( $E_{\text{corr}}$ ) and self-corrosion current density ( $i_{\text{corr}}$ ) were obtained from the PDP curves by a Tafel linear extrapolation method [43]. The corrosion rate (CR) was determined using the following equation:

$$\text{CR} = 3.27 \times 10^{-3} \frac{i_{\text{corr}} \text{EW}}{\rho}$$

Here, EW is the equivalent weight, calculated based on the relative atomic mass of Mo (95.95 g/mol) and its common valence state (6);  $\rho$  is the material density of Mo (10.28  $\text{g/cm}^3$ ). Thus, CR is simplified to  $\text{CR} = 5.09 i_{\text{corr}}$ .

Electrochemical impedance spectra of Mo were obtained from 200 kHz to 0.01 Hz with four points per frequency decade and were then fitted by a ZSimpWin (version 3.60, EChem Software, Michigan, MI, USA).

For the immersion test, the back side of Mo was sealed with epoxy resin to only expose the test area with 0.79  $\text{cm}^2$ . The sealed Mo was

immersed in 15 mL of DMEM/F-12 cell culture medium for 14 days at 37 °C, the ratio of the volume of immersion solution to area of the test sample is 20 mL/cm<sup>2</sup> according to the standard of ASTM-G31 [44]. Mo was taken out after 3, 7, and 14 days of immersion for electrochemical testing by using the same parameters described above. The surface corrosion morphology of Mo was observed using an optical microscope and a scanning electron microscope (SEM; JSM-7041F, JEOL, Tokyo, Japan). The surface elemental distribution of the corrosion products after 14 days of immersion was determined by utilizing coupled energy dispersive spectroscopy. The phase structure of the corrosion products was measured by X-ray diffraction (XRD; X'pert PRO, PANalytical, Almelo, Netherlands) at a scanning rate at 8 °/min. The bonding state and chemical composition of the surface corrosion products were tested by X-ray photoelectron spectroscopy (XPS; XSAM800, Kratos Ltd., UK) under a vacuum of  $2 \times 10^{-7}$  Pa. High-resolution C 1s, Ca 2p, Mo 3d, N 1s, O 1s, and P 2p spectra were fitted by a software of XPS peak 4.1 under a standard reference binding energy of C 1s (284.8 eV). The subsurface corrosion morphology of Mo after 14 days of immersion was imaged by the SEM after removing the surface corrosion morphology according to the standard of ASTM G1-03(2017) e1 [45]. Briefly, the samples were rinsed with deionized water, dried, and then immersed in a chemical cleaning solution consisting of 200 g/L chromium trioxide (CrO<sub>3</sub>, purity > 99 %, Chengdu Kelong Chemical Co., Ltd., Chengdu, China) at 80 °C for 1 min.

### 2.3. Cytotoxicity test

Mouse macrophage cells (RAW 264.7 cells, Procell Life Science and Technology Co., Ltd., Wuhan, China) were cultured in DMEM supplemented with 1 % penicillin/streptomycin (Gibco, Thermo Fisher Scientific, CA, USA) and 10 % fetal bovine serum (FBS; Gibco, Thermo Fisher Scientific, CA, USA) in a 5 % CO<sub>2</sub> humidified atmosphere at 37 °C.

#### 2.3.1. Cytotoxicity test of extracts test with molybdenum

According to ISO 10993-12:2021 [40] and ISO 10993-5:2009 [46], samples were immersed in cell culture medium to obtain extracts, with a sample surface-area-to-volume ratio set at 3 mL/cm<sup>2</sup>. After 72 h, Mo extracts were collected and diluted to different concentrations (100 %, 50 %, 25 %, and 10 %). Ti and copper (Cu) were used as the negative and positive control groups, respectively. Subsequently, RAW 264.7 cells were seeded in 12-well plates at a density of  $3 \times 10^4$  cells/cm<sup>2</sup> for 24 h. The medium was then replaced with extracts and cultured for 24 h. To qualitatively assess the cytotoxicity of the extracts, the macrophages were stained by live/dead cell fluorescent staining kit (Elabscience, Wuhan, China), observed under a fluorescence microscope (Olympus, Tokyo, Japan) to assess cell morphology and proliferation.

To quantitatively analyze the cytotoxicity of the extracts, relative cellular metabolic activity and relative lactate dehydrogenase (LDH) release were measured using the CCK-8 assay kit (Dojindo, Kumamoto, Japan) and LDH release assay kit (Beyotime, Jiangsu, China), respectively. Specifically, RAW 264.7 cells ( $3 \times 10^4$  cells/cm<sup>2</sup>) were seeded into 96-well plates (Corning, NY, USA) under cell culture conditions for 24 h and then the medium was removed. RAW 264.7 cells were incubated in Mo extracts with different diluted concentrations for 24 h. At the appointed times, cell culture medium containing 10 μL of CCK-8 reagent was added to each well and cultured in an incubator for 2 h. Absorbance was measured at 450 nm using a microplate reader (BioTek Instruments, Winooski, VT, USA). The relative metabolic activity was analyzed using the formula as previously reported [47]. For the LDH release assay, after preparing the working reagent, the assay was performed according to the manufacturer's instructions. The relative metabolic activity and LDH release were analyzed using the formula as previously reported [48,49].

#### 2.3.2. Cytotoxicity of direct contact test with molybdenum

The cytotoxic effect of raw and pre-treated Mo after sterilization was

evaluated by direct contact test. In brief, the specimens were placed into a 24-well plate and seeded onto the sample surface by adding 2 mL of cell suspension at a density of  $3 \times 10^4$  cells/cm<sup>2</sup>. After 24 h of incubation, the samples were removed and gently rinsed with phosphate-buffered saline (PBS). The cells were scraped off using a cell scraper, then resuspended and transferred to a 96-well plate. The CCK-8 reagents were added to the test wells, and the absorbance was measured as mentioned above. Additionally, the morphology and proliferation of macrophages on the sample surface were assessed using a live/dead cell fluorescent staining kit, followed by observation under an orthogonal fluorescence microscope.

### 2.4. Macrophage polarization phenotype

#### 2.4.1. Bright-field imaging and calcium staining of macrophages

Based on the experimental procedures described in Section 2.3.2, bright-field imaging and calcium staining of macrophages surrounding the metal were performed. After 24 h of incubation, cells were stained using 2 μM Calcein-AM (Elabscience, Houston, TX, USA) for 20 min. Cells were then observed with an orthogonal fluorescence microscope (Optiphot-2, Nikon, Tokyo, Japan). The polarization morphology of macrophages was qualitatively assessed using ImageJ software (Version 1.53, National Institutes of Health, Bethesda, MD, USA). After calibrating the measurements with a scale bar, the length, width, and perimeter were measured. The cell circularity was calculated based on previous formula [50].

#### 2.4.2. Flow cytometry, ICP-MS, and ELISA

To quantitatively assess the effect of Mo on macrophage polarization, RAW 264.7 cells were co-cultured with the Mo samples with and without pre-treatment (P-Mo and R-Mo, respectively). The cells co-cultured with Ti-based alloys were set as a negative control. Specifically, RAW 264.7 cells were seeded in 12-well plates containing the specimens at a density of  $3 \times 10^4$  cells/cm<sup>2</sup> and allowed to adhere overnight. The cells were treated with 50 ng/mL lipopolysaccharide (LPS, Sigma-Aldrich, St. Louis, MO, USA) for 24 h and set as the M1 polarization group. For M2 polarization, RAW 264.7 cells were treated with 20 ng/mL recombinant murine interleukin 4 (IL-4, Peprotech, Rocky Hill, NJ, USA) for 24 h in cell culture conditions.

At the time points of the experiment, RAW 264.7 cells surrounding the specimens were collected for subsequent flow cytometry analysis. In brief, cells around the samples were gently scraped and washed twice with cold PBS, then resuspended in 50 μL of PBS. RAW 264.7 cells were stained with 5 μL of M1 marker (APC anti-mouse CCR7 antibody; BioLegend, San Diego, CA, USA) and 1.25 μL of M2 marker (PE anti-mouse CD206 antibody; BioLegend) fluorophore-conjugated antibodies for 30 min at 4 °C in the dark. Stained cells were analyzed on a flow cytometry instrument (DxFLEX, Beckman Coulter, CA, USA). A minimum of 10,000 events were collected per sample. Flow cytometry data were analyzed using FlowJo software (Tree Star, Ashland, OR, USA). Compensation was performed using single-stained controls, and gating strategies were established using appropriate isotype controls. M1 polarization was assessed by the expression of CCR7, whereas M2 polarization was assessed by the expression of CD206.

The concentration of Mo ions in the cell supernatant and suspension were assessed using inductively coupled plasma mass spectrometry (ICP-MS, Shimadzu, Kyoto, Japan) and IL-6 concentrations in the cell supernatant were tested by ELISA assay kit (Elabscience, Wuhan, China). The content of Mo in the cell suspension represents its intracellular concentration.

#### 2.4.3. RNA isolation and RT-qPCR

To assay M1-related and M2-related RNA expression, cellular RNA was isolated using a kit according to the manufacturer's instructions (Beyotime, Shanghai, China). RNA quality/concentration was quantified using a Nanodrop spectrophotometer (Thermo Scientific) and/or an

Agilent bioanalyzer (Agilent Technologies, Santa Clara, CA, USA). Samples were stored at  $-80^{\circ}\text{C}$  prior to analysis. cDNA was generated from 500 ng of RNA per sample using oligo (dT) 12–18 primers and Superscript III (Life Technologies, Carlsbad, CA, USA) according to the manufacturer's instructions. cDNA was analyzed on an Applied Biosystems 7900 RT-qPCR instrument using  $0.5\ \mu\text{M}$  of the gene of interest. The primer sequences for the SybrGreen primer set are shown in Table S1. The expression of target genes was normalized using GAPDH as a loading control. Real-time PCR data were analyzed using the comparative Ct ( $\Delta\Delta\text{CT}$ ) method (ABI sets) or the standard curve method (mFpr2).

#### 2.4.4. mRNA sequencing and bioinformatics analysis

Following the experimental steps in Section 2.3.2, cells within a 2-mm range around the metals were collected for bulk RNA-seq. The 'limma' package in R software was utilized to identify differentially expressed genes (DEGs) in the RNA-seq dataset [51]. This resulted in the identification of all genes with a fold-change  $> 2$  as DEGs. The volcano plot was produced using the 'ggplot2' package [52]. To study the role of DEGs, Gene Ontology (GO) and Kyoto Encyclopedia of Genes and Genomes (KEGG) enrichment analyses were conducted using the DAVID database. A statistically significant cut-off points of  $p < 0.05$  was applied to determine significant enrichment.

Protein–protein interaction (PPI) network construction and module analysis were performed using the STRING database (v11.5, <https://string-db.org>), an online tool that retrieves interacting genes and proteins and builds interaction networks [53,54]. Genes with a total score of  $> 0.4$  were selected for network construction. The resulting networks were visualized using Cytoscape software (v3.8.2, <https://cytoscape.org>) [55].

#### 2.4.5. Inhibitor and immunofluorescence staining

The matrix metalloproteinase 9 (MMP9) inhibitor Ilomastat (HY-15768; Medchemexpress, Shanghai, China) was used to treat RAW 264.7 cells to inhibit MMP9 activity. The application of Ilomastat was performed as previously described [56–58]. Briefly, RAW 264.7 cells were seeded on glass coverslips in a 6-well plate at a density of  $2 \times 10^6$  cells/mL and allowed to adhere overnight. Cells were then treated with  $20\ \mu\text{M}$  Ilomastat for 24h, followed by raw Mo. Cells were fixed with 4 % paraformaldehyde in PBS for 10 min at room temperature, and then washed with 0.1 % Triton X-100 three times. Cells were incubated with anti-actin (Beyotime, Cat# C1036, Shanghai, China) diluted in 1 % BSA in PBS at room temperature for 40 min, 4',6-diamidino-2-phenylindole (DAPI) for 5 min, and then washed three times with PBS. Coverslips were mounted on glass slides. RAW 264.7 cells were stained with DAPI (blue) to visualize the nuclei and with a phalloidin-conjugated fluorophore (red) to stain the cytoskeleton. Images were captured using a fluorescence microscope equipped with appropriate filters at  $40 \times$  magnification. Analysis of fluorescence was performed using ImageJ software.

### 2.5. Statistical analysis

All numerical data were given as mean and standard deviation (SD). Prior to statistical analysis, the normality was assessed by a Shapiro-Wilk test. Where applicable, the parametric data sets were evaluated by one-way analysis of variance (ANOVA) with Tukey's multiple comparisons test, non-parametric datasets were evaluated by the Kruskal-Wallis test with Dunn's multiple comparisons test. All statistical analyses were performed by GraphPad PRISM software version 9 (GraphPad Software, Inc., San Diego, USA). Statistical significance was defined as a  $p$ -value less than 0.05.

## 3. Results

### 3.1. Electrochemical analysis of molybdenum

The *in vitro* corrosion behavior of pure Mo in DMEM/F-12 medium was assessed (Fig. 1). The  $E_{\text{corr}}$  value of Mo shifted to more negative direction with the prolonged immersion time (Fig. 1a). In the high anodic overpotential region, transient current peaks were observed, likely related to the dynamic formation and degradation of the surface oxide layer, a phenomenon also reported in previous studies [35]. The corrosion rate of Mo, determined by the  $i_{\text{corr}}$  value, was  $4.68 \pm 0.25\ \mu\text{m}/\text{year}$  after 14 days of immersion. The Nyquist impedance spectrum of Mo consisted of two capacitive loops; the impedance value decreased with increasing of immersion time (Fig. 1b). Bode-impedance (Fig. 1c) exhibited a similar trend to the Nyquist spectra. To further analyze the EIS spectrum, the equivalent circuit (EEC) diagram of  $R_s(Q_p(R_p(Q_{dl}(R_{ct})))$ . Where  $R_s$  stands for the resistance of Hank's solution.  $Q_p$  and  $R_p$  denote the capacitance and resistance of the surface oxide layer, while  $Q_{dl}$  and  $R_{ct}$  are related to the double layer capacitance and the resistance associated with the interfacial charge transfer reaction. The fitting data was shown in Table S2 (Supplementary Materials), Mo illustrated lower  $R_p$  and  $R_{ct}$  values after immersion, which may be related to the dynamic evolution of its surface corrosion products. This will be discussed in detail later.

Optical images showed that the surface color of Mo was significantly changed following immersion (Fig. 1d). Specifically, the color changed from gray (3 days) to dark yellow (7 days), and ultimately to black (14 days). Additionally, randomly distributed granular corrosion products were observed by SEM, and shown by energy dispersive spectroscopy to be composed of Mo, P, O, Ca, and C (Fig. 1d). XRD patterns of Mo before and after immersion (Fig. 1e) showed the characteristic peaks of Mo and  $\text{MoO}_2$  on all samples. Note the  $\text{MoO}_2$  peak in pure Mo was ascribed to the corrosion layer formed in air. The characteristic peak of  $\text{MoO}_3 \cdot 2(\text{H}_2\text{O})$  appeared in the samples after 14 days of immersion. XPS after 3, 7, and 14 days of immersion (Fig. 1f) indicated the presence of O 1s, N 1s, C 1s, Mo 3d, and P 2p in all samples. High-resolution XPS of C 1s showed the peaks of C-C, C-O, and C-N/C=N (Fig. 1g), whereas Ca 2p spectra detected  $\text{Ca}^{2+}$  not until after 7 and 14 days of immersion (Fig. 1h). From the Mo 3d spectra, Mo,  $\text{Mo}^{4+}$ , and  $\text{Mo}^{6+}$  were detected (Fig. 1i). In the N 1s curve (Fig. 1j), the N=C and N-C were observed. From the O 1s spectra (Fig. 1k), the O-Mo, -OH, and  $\text{H}_2\text{O}$  were detected; O-Mo might be associated with the coordination reaction between organic molecules in DMEM/F-12 and Mo ions.  $\text{PO}_4^{3-}$  ions were also detected from the P 2p spectra (Fig. 1l). The subsurface morphology of Mo after removing corrosion products showed no significant localized or pitting corrosion from the optical images but some pits appeared in the SEM images (Fig. S1); this was attributed either to the possible slight localized pitting corrosion of Mo or to the pitting casting a defect caused by the sintering process.

### 3.2. Extract test and direct contact test

To assess the cytotoxicity of Mo *in vitro*, extract test and direct contact experiments were performed (Fig. 2a). The representative fluorescence staining images of live/dead cells cultured in extracts were showed a large amount of green fluorescence (live cells) in the negative control, with almost no red fluorescence (dead cells), whereas all concentrations of Mo extracts demonstrated acceptable cell cytocompatibility (Fig. 2b). The macrophages exhibited a round shape and grew in clusters. According to ISO 10993-5: 2009 [46], the inhibition of mean cell metabolic activities was above 30 % ( $< 70\%$  of control), indicating cytotoxic effects. CCK-8 results showed that the relative cell metabolic activity for all concentrations of Mo extracts was  $> 70\%$  of the control, indicating no cytotoxic effects (Fig. 2c). Cell supernatants were used in LDH assays to test the amount of LDH released by cells into the extracellular space to assess cell membrane damage. Cell membrane damage



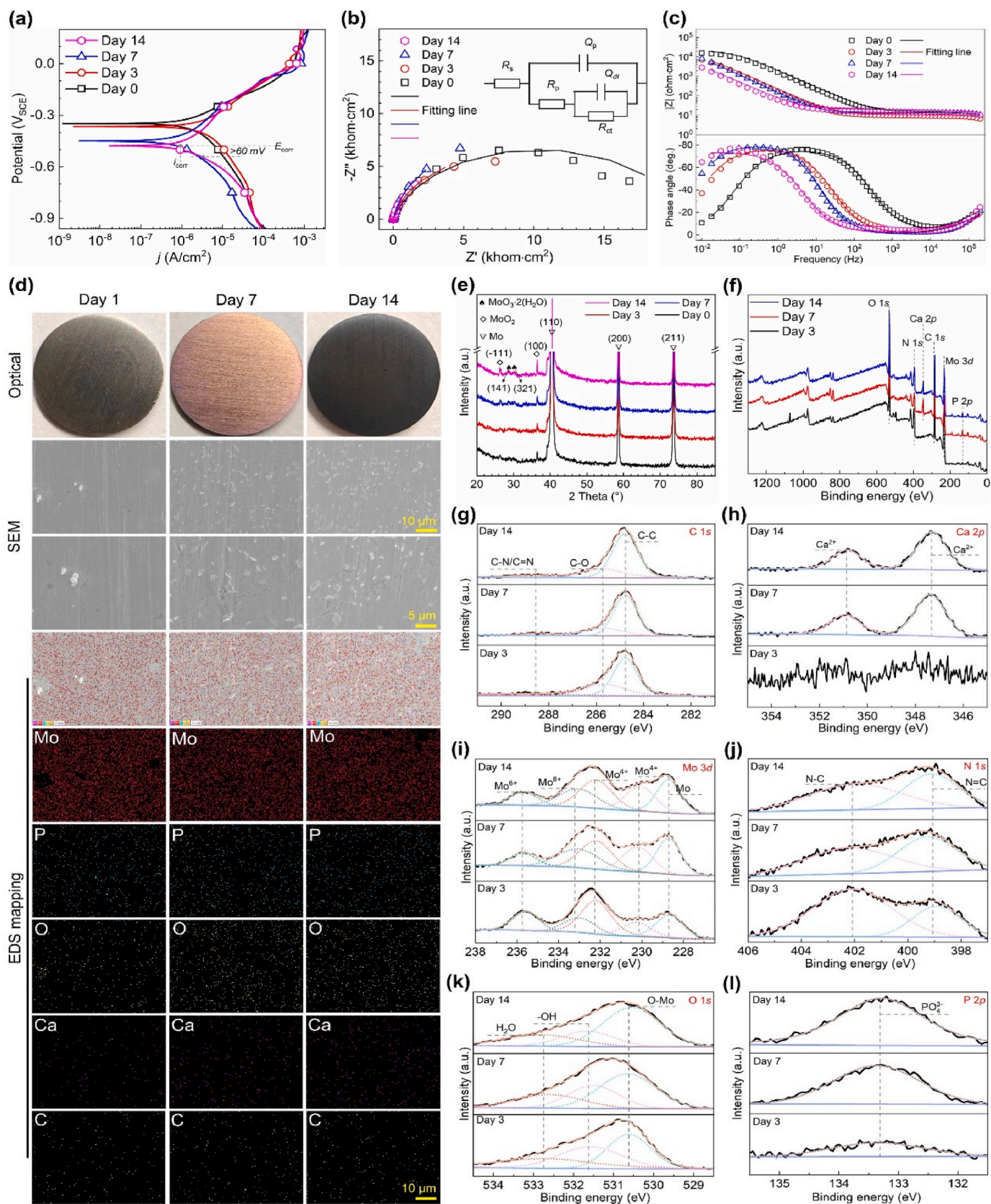


**Fig. 1.** *In vitro* corrosion behavior of pure molybdenum before and after 3, 7, and 14 days of immersion in DMEM/F-12 medium at 37 °C. (a) Potentiodynamic polarization (PDP) curves. (b) Nyquist plots embedded with equivalent circuit diagram. (c) Bode-impedance and Bode-phase angle spectra. (d) Representative optical and SEM images of Mo after immersion. (e) X-ray diffraction (XRD) patterns. (f) X-ray photoelectron spectroscopy (XPS) survey. (g)–(l) High-resolution XPS spectra of C 1s, Ca 2p, Mo 3d, N 1s, O 1s, and P 2p, respectively.

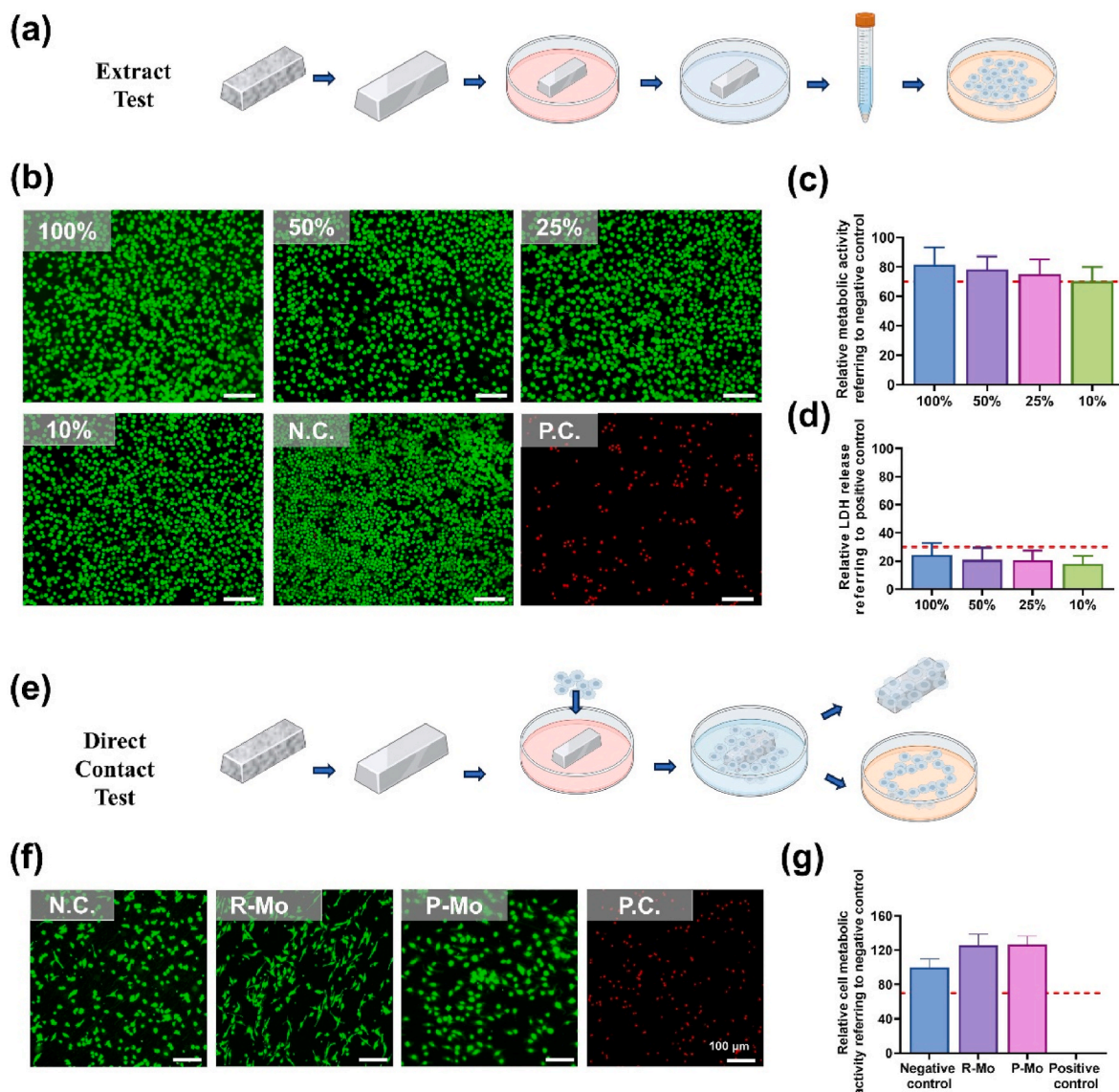


**Fig. 2.** *In vitro* cytocompatibility results. (a) Schematic diagram illustrating extract test (created by [biobender.com](#)). (b) Representative fluorescence images (scale bar = 100 μm, magnification 200 ×) of RAW 264.7 cells stained with live-dead staining after 24-h of exposure to Mo extracts. (c) CCK-8 assay to determine relative metabolic activity. The red dashed line represents the cut-off between toxic and non-toxic results (70 % of the negative control). (d) The LDH assay determines the amount of LDH released by the cells into the cell supernatant. The red dashed line represents the cut-off between toxic and non-toxic results (30 % of the positive control). (e) Schematic diagram illustrating direct contact experiments (created by [biobender.com](#)). (f) Representative fluorescent image of RAW 264.7 cells after exposure to Mo for 24 h and staining of the metal by live-dead staining (Scale bar = 100 μm, magnification 200 ×). (g) LDH assay to determine relative metabolic activity. The red dashed line represents the cut-off between toxic and non-toxic results. The N.C. and P.C. represent negative control and positive control, respectively. (For interpretation of the references to color in this figure legend, the reader is referred to the Web version of this article.)

was not affected by changes in the mass volume fraction of the leachate dilution compared to the positive control (Fig. 2d), in agreement with CCK-8 results. Furthermore, no significant differences in cell metabolic activities and LDH release were observed between different tested groups ( $p > 0.05$ ), determined by the Kruskal-Wallis test with Dunn's multiple comparisons test.

In addition, the cytotoxicity of Mo was assessed by direct contact of macrophages with the metals (Fig. 2e). Representative fluorescence images of macrophages directly adhered to the sample surfaces indicated dead cells on the Cu surface, indicating compromised membrane integrity in apoptotic RAW 264.7 cells (Fig. 2f). In contrast, RAW 264.7 cells adhered to the R-Mo and P-Mo groups displayed green fluorescence, indicating cell membrane integrity. These results were comparable to those observed in the negative control. Notably, RAW 264.7 cells adhered on the R-Mo surface showed more cellular pseudopods

compare to negative control. To further quantitatively analyze the metabolic activity of macrophages exposed to the sample surfaces, the cell relative cellular metabolic activity of both P-Mo and R-Mo groups was shown to be within the ISO 10993-5: 2009 standard (> 70 % of control), while the positive control group (Cu group) showed a significant decrease in cell relative metabolic activity (Fig. 2g). In summary, both the extract test and the direct contact test showed that pure Mo had no adverse effects on cell viability.

### 3.3. Effect of molybdenum on macrophage morphology and polarization

Bright-field micrographs and FITC-channel calcium staining images of macrophages surrounding the samples were obtained after co-culturing RAW 264.7 cells with the specimens for 24 h (Fig. 3a). In the R-Mo group, some cells exhibited spindle-shaped, elongated



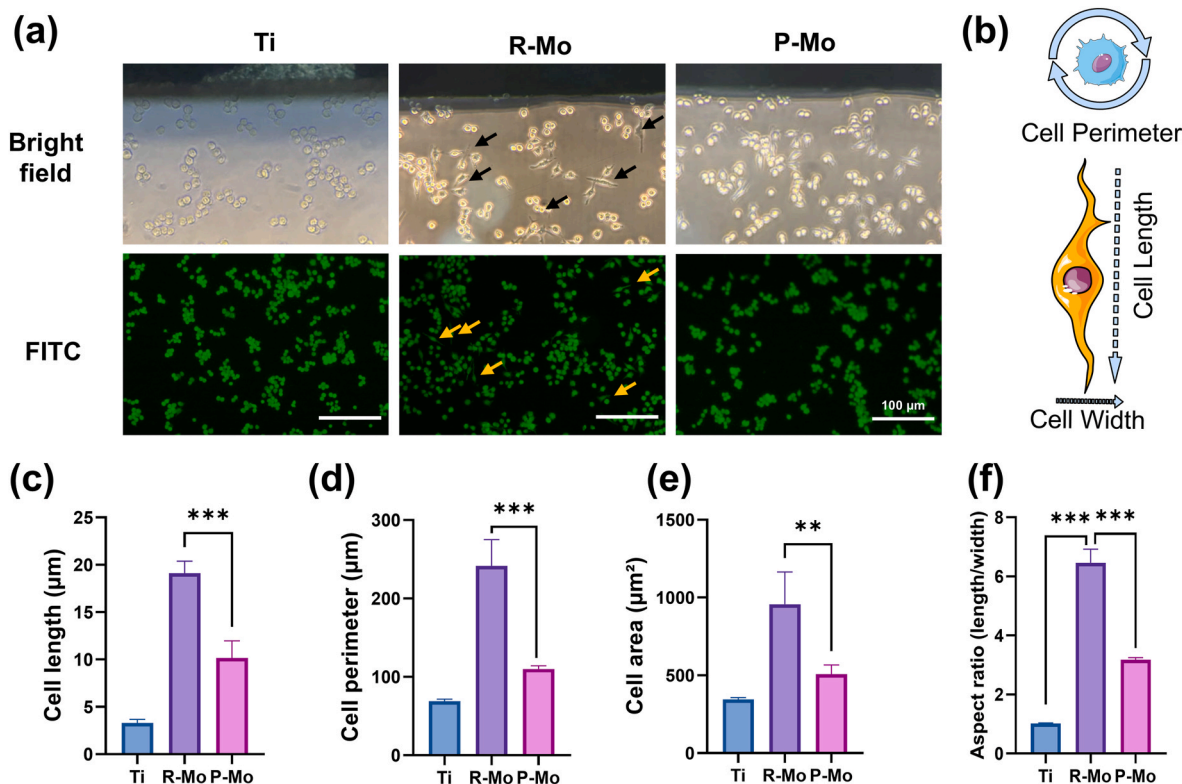


**Fig. 3.** Effect of molybdenum on the morphology of RAW 264.7 cells. (a) Representative Bright-field photomicrographs and FITC channel calcium-stained fluorescence microscopic images of peripheral RAW 264.7 cells cultured on Ti, R-Mo, and P-Mo (magnification 100 ×, scale bar = 100 μm). Black and yellow arrows indicate significant morphological changes in macrophages observed under microscopy. (b) Schematic diagram of macrophage measurement in the experiment. (c–f) Statistical graphs of macrophage length, perimeter, area, and aspect ratio analyzed using one-way ANOVA. \* $p < 0.05$ , \*\* $p < 0.01$ , \*\*\* $p < 0.001$ . (For interpretation of the references to color in this figure legend, the reader is referred to the Web version of this article.)

morphology with extended edges, contrasting with the regular shape in the Ti group, suggesting possible cytoskeletal rearrangements. However, calcium distribution remained consistent among three groups, indicating that cellular activity was not significantly affected. A schematic representation of macrophage morphology measurements is shown in Fig. 3b. Cell length, perimeter, area, and aspect ratio were assessed for each experimental group (cell width results are available in Fig. S2). RAW 264.7 cells in the R-Mo group showed increased length, aspect ratio, perimeter, and area surrounding the samples compared to cells in the Ti and P-Mo groups, which exhibited a more elongated shape (Fig. 3c–f).

Macrophage polarization and its cellular morphology have an indicated relationship. Therefore, macrophage polarization surface markers CCR7 (M1 surface marker) and CD206 (M2 surface marker) were assessed using flow cytometry (Fig. 4a). The P1 gate was used to identify single cells and the P2 gate was used to further identify live cells. The percentage of positive cells was analyzed using quadrant gates. The percentage of macrophage M1 and M2 polarized positive cells was plotted statistically (Fig. 4b). The proportion of positive cells for M1 polarization of macrophages increased in the R-Mo group in relation to cells in the Ti and P-Mo groups (\* $p < 0.05$ ). The concentration of IL-6 in the R-Mo group was significantly higher than that in the P-Mo group (Fig. 4c). The pH variation in the cell culture supernatant was minimal, with no significant differences observed among the Ti, R-Mo, or P-Mo groups (Fig. 4d). The concentration of Mo in the cell supernatant and suspension, as assessed via ICP-MS, was shown to be highest in the R-Mo group, while pre-treatment (P-Mo) significantly reduced the Mo concentration in both cell supernatant and intracellular (Fig. 4e).

RT-qPCR was performed for gene expression profiling of inflammation-related genes (*Tnf*, *Il6*, *Il1b*) and oxidant-related genes (*Hmox1*) (Fig. 4f). RAW 264.7 cells showed upregulation of the

expression of inflammation-related genes *Tnf*, *Il6*, and *Il1b* and of the oxidant-related gene (*Hmox1*) after 24 h of R-Mo treatment, whereas gene downregulation was observed after P-Mo treatment relative to the R-Mo group (\* $p < 0.05$ ). The concentration of Mo and IL-6 in the cell supernatant also exhibited consistent results. However, there were no statistically significant differences in gene expression of inflammation-related enzymes (*COX2*) and M2 polarization-related proteins (*Cd68*) (Figs. S3a–b).

#### 3.4. RNA-sequencing analysis of the effect of molybdenum on macrophages

By setting the cut off values of  $q$  and fold-change (FC) at 1.139 and 1.128, RNA of R-Mo-treated RAW 264.7 cells constituted of 925 genes (882 upregulated and 41 downregulated) showing differential expression between Ti-treated and R-Mo treated cells (Fig. 5a). Fig. 5b illustrates the KEGG pathway analysis of the identified genes, which are enriched in the 'HIF-1 signaling pathway' and 'Neutrophil extracellular trap formation' pathway. In DEGS, hub genes were screened using the Cytoscape software through the use of the Matthew's correlation coefficient (MCC) plug-in. Sorting by  $p$  value, GO terms of the biological process (BP); cellular component (CC) and molecular function (MF) are shown in Fig. 5c shows that the identified genes are primarily involved in the positive regulation of cell adhesion and angiogenesis in the BP category, localized to the membrane and extracellular region in the CC category, and are mainly associated with calcium ion binding and kinase activity in the MF category. PPI network diagrams were constructed to show the interactions between enriched genes (Fig. 5d and e). PPI networks show the six hub genes, namely, *Mmp9*, *Acta2*, *Nos2*, *Vegfa*, *Nos3*, *Col4a2*. The darker the color, the stronger the degree of criticality. *Mmp9*, *Acta2* (Fig. 5f and g) and *Nos2* (Fig. S4) gene expression levels

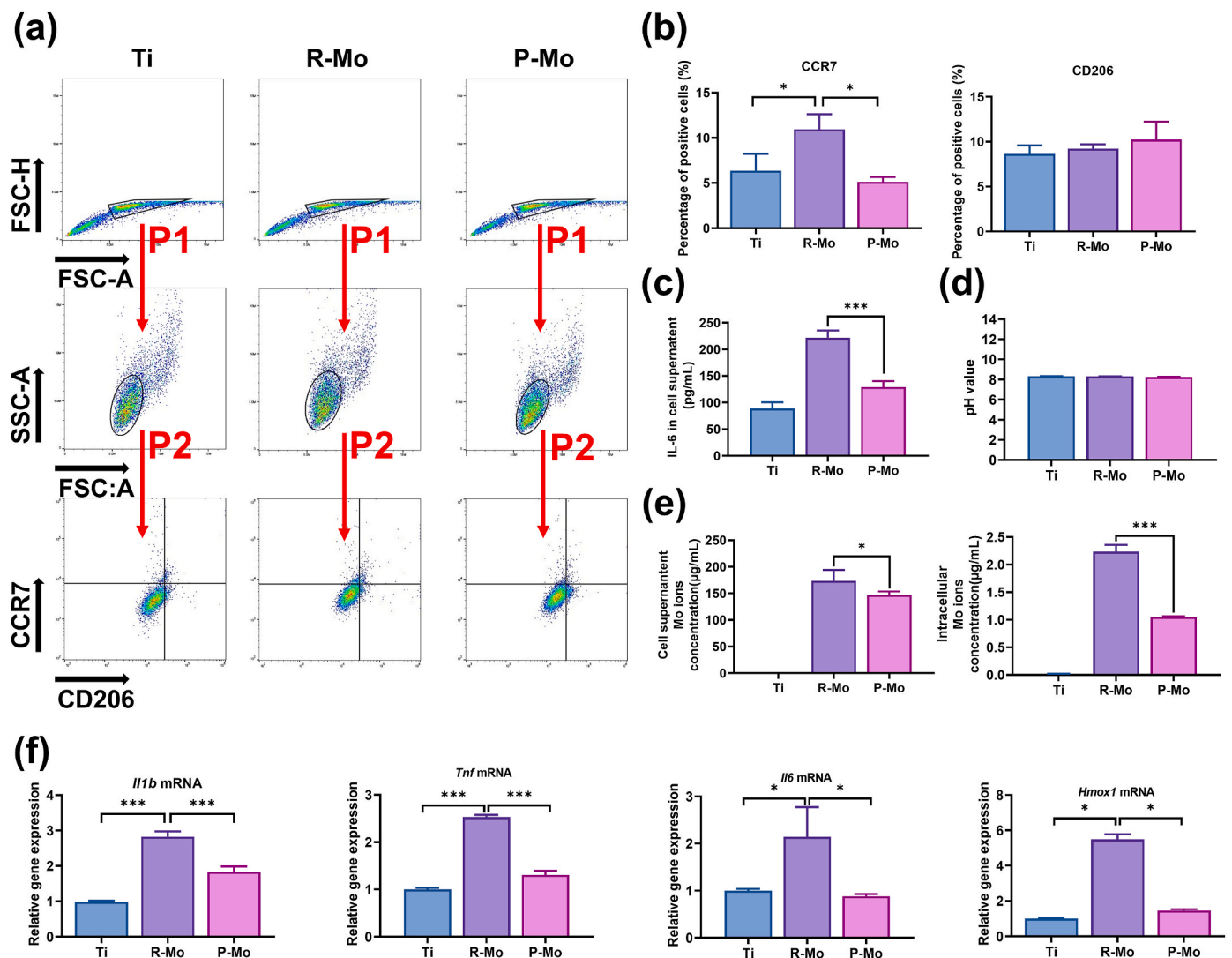


**Fig. 4.** Effect of molybdenum on the polarization of RAW 264.7 cells. (a) Flow cytometry analysis of RAW 264.7 cells cultured on Ti, R-Mo, and P-Mo treated after 24 h. (b) Statistical graph of CCR7-positive (M1 marker) and CD206-positive (M2 marker) cells. (c) Concentration of IL-6 in the cell supernatant measured using ELISA. (d) pH values of the cell supernatant. (e) Concentration of Mo ions in the cell supernatant and intracellular measured using ICP-MS. (f) RT-qPCR measurements of the expression profile of inflammatory-related genes (*Tnf*, *Il6*, and *Il1b*) and Oxidant-related genes (as *Hmox1*) after 24 h treatment by Ti, R-Mo, and P-Mo. Data were normalized to the mean values of *Gapdh* gene expression for each gene of interest. The *p*-values are based on one-way ANOVA: \**p* < 0.05, \*\**p* < 0.01, \*\*\**p* < 0.001.

within the cells were validated using RT-qPCR. The RNA expression level of *Mmp9* was more than four times higher than that in the Ti group, and its upregulation was more pronounced than that of *Acta2*.

The results of bioinformatics analysis and validation of relative gene expression levels indicate that *Mmp9* is the most prominently altered gene during the R-Mo-induced polarization of RAW 264.7 cells towards the M1 phenotype (Fig. 5). Therefore, subsequent studies focused on *Mmp9*.

### 3.5. Effect of raw molybdenum on macrophages treated by MMP9 inhibitor

To further verify the critical role of *Mmp9* in the induction of M1 polarization by raw Mo, MMP9 inhibitors were used to pre-treat RAW 264.7 cells. Phalloidin staining and DAPI staining were used to visualize the cytoskeleton (red) and nuclei (blue) of RAW 264.7 cells in the R-Mo group and after pre-treatment with the MMP9 inhibitor (Ilomastat) (Fig. 6a). In this experiment, the group pre-treated with Ilomastat alone was set as the negative control. The cell circularity corresponded to the

observed cell morphology (Fig. 6b). By calculating the circularity of macrophages, the roundness of cells treated with the inhibitor was closer to 1. However, the value for the R-Mo group was less than 0.5. Treatment with an MMP9 inhibitor reduced the expression of *Il6*, *Il1b*, and *Hmox1* in RAW 264.7 cells surrounding the raw Mo (Fig. 6c).

## 4. Discussion

Metallic Mo demonstrates excellent mechanical properties and biocompatibility, making it a promising candidate for medical implants. Understanding the mechanisms by which Mo induces inflammatory or immune responses is essential for its clinical translation. The degradation behavior of metallic Mo is influenced by physiological conditions [59]. According to the results presented herein, the primary degradation products of pure Mo in DMEM/F-12 medium during *in vitro* corrosion include Mo, P, O, Ca, and C. Additionally, XRD results indicate that the degradation process of Mo is primarily concentrated around the characteristic peaks of Mo and MoO<sub>2</sub>. The biocompatibility of Mo on macrophages has been effectively verified. Furthermore, bioinformatics



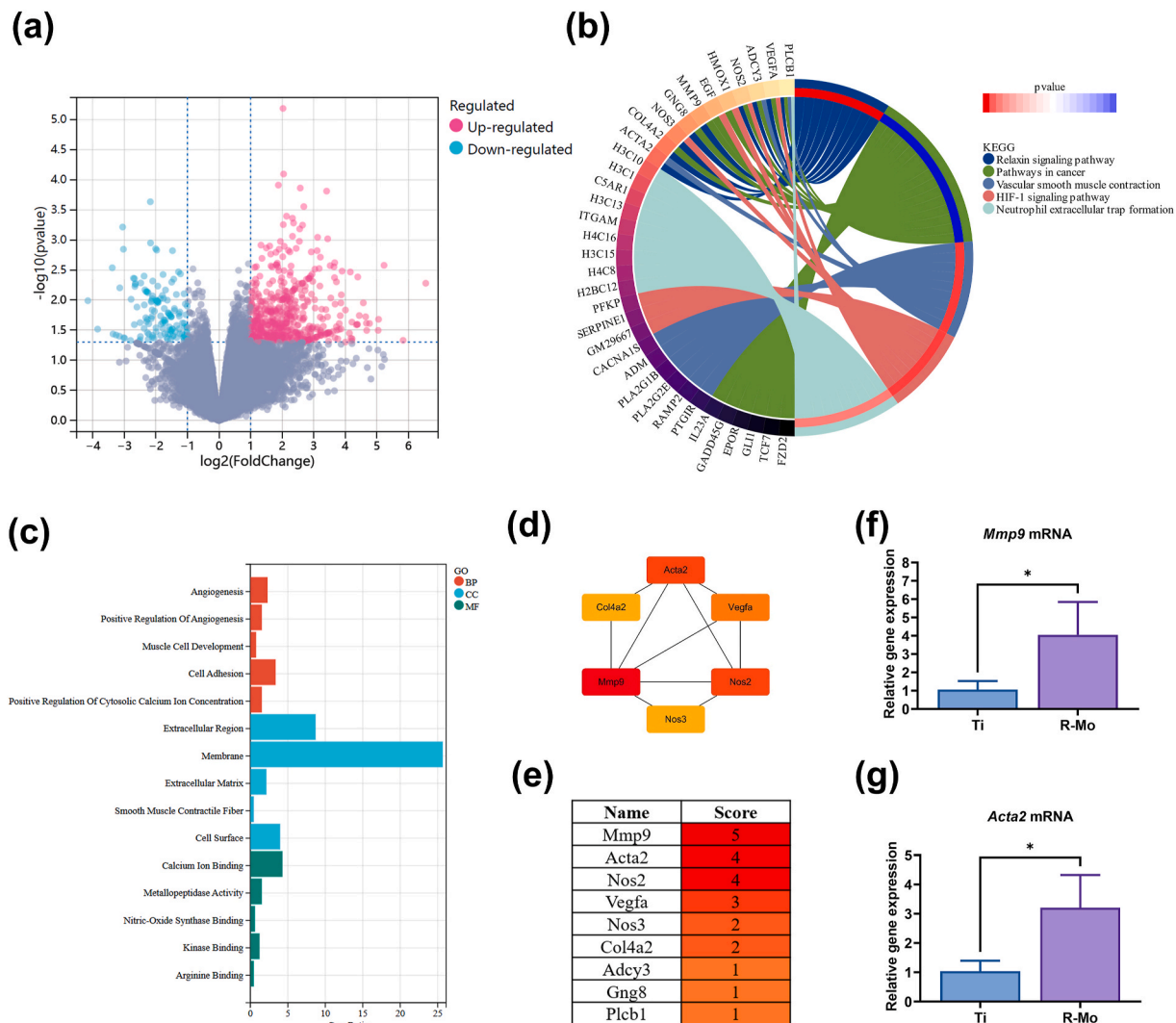
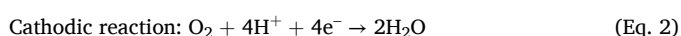


**Fig. 5.** Identification of differentially expressed genes, gene set enrichment analysis and RT-qPCR validation. (a) Volcano plot of differentially expressed genes (DEGs). There were 925 differentially expressed genes, consisting of 41 downregulated genes and 882 upregulated genes. (b) Kyoto Encyclopedia of Genes and Genomes (KEGG) pathway enrichment of the union of R-Mo-treated regulator pathways. (c) Gene ontology (GO) enrichment analysis of R-Mo treated RAW 264.7 cells; biological process (BP); cellular component (CC); molecular function (MF). (d) and (e) Functional proteins and their scores were analyzed through molecular complex detection (MCD) in protein-protein interaction (PPI) analysis. Hub genes in DEGs were screened using the matthew's correlation coefficient (MCC) plugin in Cytoscape software. (g) RT-qPCR validation of top 2 enriched genes as *Mmp9* and *Acta2*. The *p*-values are based on one-way ANOVA: \**p* < 0.05.

analysis and validation experiments suggest that the *Mmp9* gene and related pathways play an important role in the Mo-induced polarization of macrophages towards the M1 phenotype.

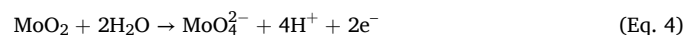
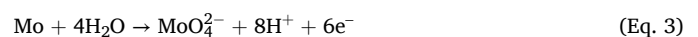
#### 4.1. Degradation behavior under physiological conditions

According to thermodynamic charts, Mo corrosion occurs through an oxygen-consuming reaction, similar to the corrosion processes of Zn, Fe, and their alloys [38,60,61]. In contrast, the corrosion of Mg and its alloys, another commonly used as biodegradable metals, is characterized by a hydrogen evolution reaction [48]. From a thermodynamic perspective, Mo in a neutral environment, including the DMEM/F-12 solution used in this study, tends to passivate and form a  $\text{MoO}_2$  oxide layer during the initial stages of corrosion [11,35,38,62]. Specifically, the process can be described by the following equations:



The corrosion of Mo is a cascade reaction, wherein the surface

corrosion products of Mo continuously evolve during the corrosion process. As corrosion progresses, the surface corrosion products transition from lower oxidation states to higher oxidation states, eventually dissolving into molybdate ions. This process can be explained by the following equations:



The degradation process of Mo and the changes in surface elements during immersion in DMEM/F-12 solution were investigated and analyzed using electrochemical methods (Fig. 1). Results from the PDP curves showed that the corrosion potential shifted in a negative direction with prolonged immersion time, which may be attributed to changes in the type of the surface corrosion product layer. A previous study has suggested that the potential difference between the oxidation reaction (anode) and reduction reaction (cathode) increases as the

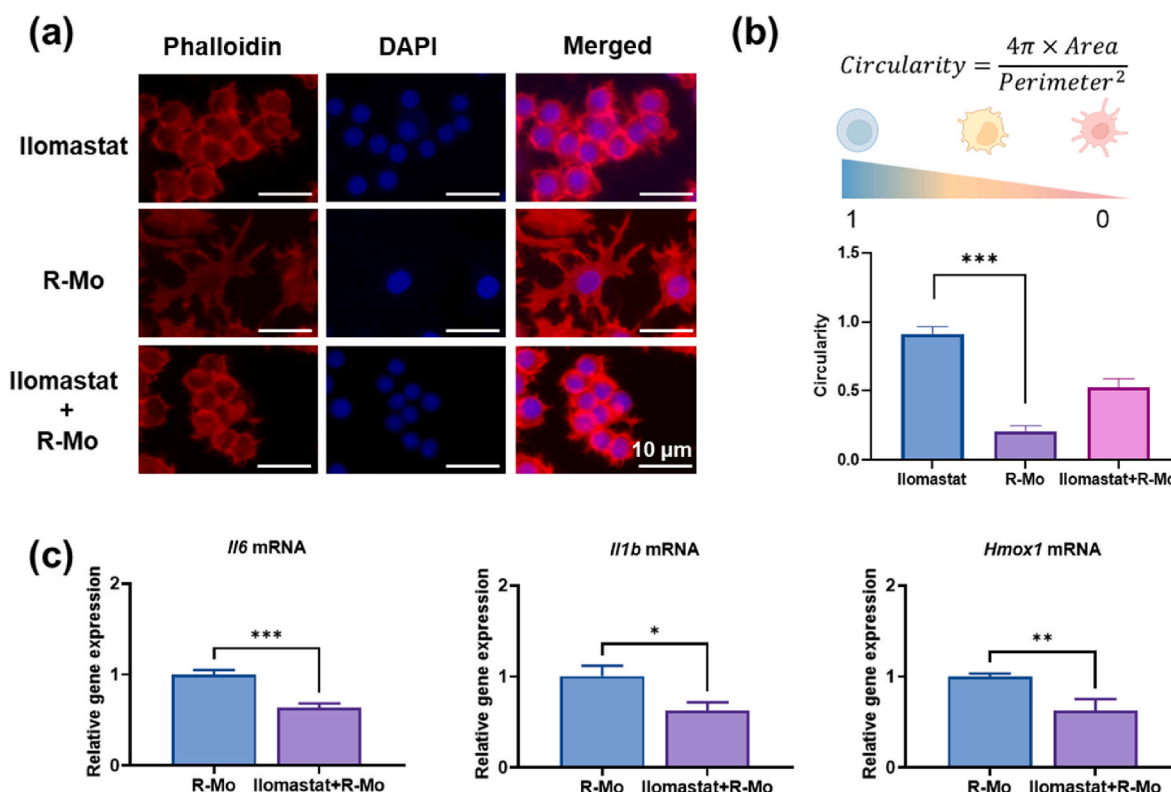


**Fig. 6.** Effect of raw molybdenum on RAW 264.7 cells treated with MMP9 inhibitor (Ilomastat). Images were captured using a confocal microscope at 60  $\times$  magnification. Scale bar = 10  $\mu\text{m}$ . (b) Cell circularity formula and schematic diagram (created by [biorender.com](#)), followed by the corresponding analytical results of macrophages. (c) RT-qPCR analysis of gene expression levels. Expression of *Il6*, *Il1b*, and *Hmox1* genes in treated versus R-Mo treated RAW 264.7 cells. Data are presented as mean  $\pm$  standard error of the mean (SEM) from three independent experiments. Expression levels were normalized to *Gapdh*. Statistical significance are based on one-way ANOVA: (\* $p < 0.05$ , \*\* $p < 0.01$ , \*\*\* $p < 0.001$ ).

corrosion products of Mo transition from a low valence state to a high valence state [11], resulting in a negative potential shift. Corrosion products on the surface of Mo are primarily oxides that exhibit semiconductor properties. As the valence of Mo increases, the bandgap of these oxides widens:  $\text{MoO}_{3-x}$  ( $2 < x < 3$ ) exhibits high conductivity,  $\text{MoO}_2$  is classified as semi-metal, and  $\text{MoO}_3$  has a wide bandgap ( $> 2.7$  eV) [63]. The color of Mo surface products changes as it transitions from a low valence state to a high valence state, typically from gray to yellow, and eventually to black or even transparent [11,38], which aligns with the observations above. Importantly, XRD further confirmed that high-valence oxides of Mo ( $\text{MoO}_3$ ) were detected only after 14 days of immersion. XPS results also showed the presence of Mo ions in different valence states. Thus, the corrosion products on the surface of Mo undergo dynamic changes during immersion in DMEM/F-12 cell medium, transitioning from low-valence oxides to high-valence oxides.

The different valence of Mo oxide may induce different cell responses on macrophages. Mo ions ( $\text{MoO}_4^{2-}$ ) can influence the formation of multinucleated giant cells *in vivo* to modulate the polarization type of macrophages [64]. In addition, recent studies have confirmed the functionality of other Mo corrosion products, such as  $\text{MoO}_2$  and  $\text{MoO}_3$ , on osteoblasts and osteoclasts, demonstrating their ability to promote osteogenic differentiation and inhibit osteoclast activity in a concentration-dependent manner [65,66]. However, to the best of our knowledge, no study has explored the relationship between these corrosion products and macrophage behavior, despite this being a crucial factor in the clinical translation of Mo-based implants.

#### 4.2. Assessment of macrophage responses towards metallic molybdenum

Cytocompatibility, hemocompatibility, and biocompatibility are critical for the use of degradable implants [67–69]. These criteria ensure

that biomaterials interact effectively with human cells, blood components, and major organs, which is essential for their materials properties of medical implants. The effects of Mo on macrophages were assessed in terms of morphology, metabolism, gene expression levels, and RNA transcription to reveal the mechanisms and potential targets of Mo-induced transformation of RAW 264.7 cells towards M1 polarization. In this study, both the direct and indirect cell experiments confirmed that Mo exhibits no significant cytotoxicity to macrophages. It should be emphasized that the Mo implants trigger an immune response upon implantation. As the first responders in the immune process, macrophages are recruited to the vicinity of the implant, where the corrosion products released during Mo degradation could impact immune cells. To simulate this process, we employed an *in vitro* model wherein the macrophages were co-cultured with the specimens. Mo exhibited biocompatibility comparable to Ti, which is regarded as the gold standard for metallic implants, consistent with Toschka's study [28]. However, raw Mo was shown to affect the morphology of RAW 264.7 cells rounding and elongated the cells. In contrast, Mo treated by media immersion did not cause this effect in RAW 264.7 cells (Fig. 3). Further, flow cytometry experiments confirmed the raw Mo-induced polarization of macrophages toward M1 phenotype (Fig. 4a and 4b). M1 polarization of macrophages is considered indicative of a pro-inflammatory state [70], indicating that Mo has the potential to induce localized cellular inflammation, consistent with the findings by Sikora-Jasinska et al. [31].

Furthermore, P-Mo was shown to reduce the concentration of Mo ions, so as cytokine IL-6 released by macrophages. These results showed elevated changes in both inflammation-related genes (*Tnf*, *Il6*, and *Il1b*) and oxidation-related genes (*Hmox1*) (Fig. 4f and Fig. S3). Schauer et al. conducted a study using a rat model to analyze the concentration of Mo ions in rat organs following the implantation of Mo devices [71]. They

showed that a significant amount of Mo was found near the implant site, while Mo levels in other organs did not increase, similar to our findings (Figs. 2 and 3). This suggests that Mo may primarily affect the surrounding tissues or cells rather than distant ones.

The early-stage release of Mo ions is a critical intervention. According to our experimental results, *in vitro* system, Mo exhibits acceptable effect on macrophage cell viability (Fig. 3). However, untreated raw Mo exposes surrounding macrophages to relatively high concentrations of Mo, leading to increased intracellular Mo levels. This suggests that the early degradation of Mo impacts the local immune environment, a phenomenon that warrants further study. Based on the analysis of macrophage morphology (Fig. 3), Mo ion concentration (Fig. 4e) and gene expression (Fig. 4f), this study demonstrates that preconditioning of Mo is an effective strategy to control the early-stage release of Mo ions.

#### 4.3. Potential mechanism of macrophage M1 polarization

To investigate the mechanism by which raw Mo induces the conversion of RAW 264.7 cells to M1 polarization, RNA sequencing analysis targeted *Mmp9* (Fig. 5), and showed elevated expression of *Mmp9*. Further, inhibitors of the MMP family were used to verify that *Mmp9* gene plays an important role in the M1 polarization process of RAW 264.7 cells in this system (Fig. 6). The morphology of macrophages was closer to that of the negative control after the use of MMP9 inhibitors (Fig. 6a). The expression of pro-inflammatory genes related to their biological activity such as *Tnf*, *Il6*, and *Hmox1* gene decreased under inhibitor condition (Fig. 6c), suggesting that *Mmp9* is not only one of the markers of M1 polarization but may play an important role in raw Mo regulation of macrophage polarization.

In exploring the mechanism by which Mo induces the polarization of RAW 264.7 cells toward M1 (Fig. 7), our findings are consistent with previous studies. Yang et al. showed that, in an inflammatory

environment, MMP9 expression was increased to promote the shift of macrophages toward the M1 phenotype [72]. Inhibition of MMP9 activity significantly reduced the number of M1 macrophages, further supporting the induced role of MMP9 in M1 polarization [73]. In contrast to previous studies, our experiments further elucidated the causal role of *Mmp9* in M1 polarization through inhibitor treatment and identified potential target genes influenced by Mo metal in promoting M1 polarization in RAW 264.7 cells.

Existing studies have shown that multiple signaling pathways that regulate cellular inflammation, proliferation, and metabolism, such as NF- $\kappa$ B [74], MAPK-ERK [75], and PI3K-AKT, affect the expression of MMP9 [76]. Additionally, we have shown that multiple pathways involved in MMP9 regulation, such as HIF-1 signaling pathway and neutrophil extracellular traps formation, were enriched in R-Mo group compared to Ti (Fig. 5d), which align with previous research [77,78]. The neutrophil extracellular trap formation pathway plays a crucial role in regulating immune defense, immune responses, and wound healing [79]. More importantly, based on current studies, the HIF-1 signaling pathway plays a crucial role in regulating tissue repair and regeneration, particularly in maintaining cellular oxygen balance [80]. The potential oxidative degradation process of Mo in the *in vivo* environment likely affects cellular oxygen balance, activating the HIF-1 signaling pathway and inducing *Mmp9* gene expression, which triggers macrophage polarization towards the M1 phenotype (In Section 4.1). Thus, enrichment of the neutrophil extracellular trap formation pathway suggests that the 'neutrophil-macrophage' immune environment during the Mo degradation process merits further investigation.

Furthermore, the cellular component may be responsible for R-Mo-induced macrophage polarization. Scavenger receptors and metal transport protein 1 on cell membranes have been demonstrated to be modulated by metal ions to influence oxidative stress [81], cell metabolism [82], and inflammation [83]. Based on the RNA sequencing results and existing studies, we could propose that Mo-related proteins

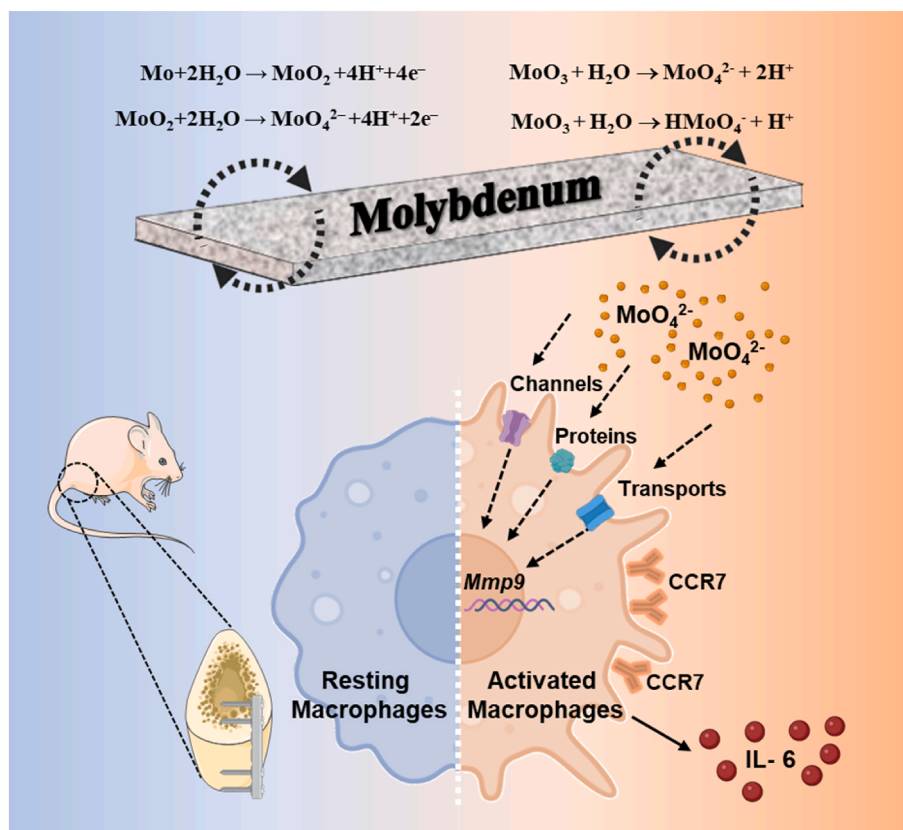


Fig. 7. Schematic representation of macrophage-related inflammatory responses to degradation products of biodegradable molybdenum implants.

may enter cells through the cellular membrane via these two mechanisms, leading to elevated *Mmp9* gene expression and subsequently inducing M1 polarization.

Although the present study revealed an important role of *Mmp9* in Mo-induced macrophage polarization, validation in future *in vivo* model studies remains necessary as the present study is based mainly on *in vitro* experiments. Furthermore, Mo occurs principally in the VI oxidation state as molybdate ( $\text{MoO}_4^{2-}$ ) ions [38,84,85]. However, Mo also exists in divalent and tetravalent states. Therefore, whether the valence states of Mo are involved in regulating the immune environment remains unclear. Future research will focus on investigating Mo's applications in the medical field, aiming to explore the findings of this study and resolve existing limitations.

## 5. Conclusions

In this study, the biodegradation behavior of metallic Mo and its effects on macrophage M1 polarization were explored using electrochemical analysis and *in vitro* experiments. The early degradation of Mo was found to modulate the morphology and polarization of nearby macrophages towards an M1 phenotype, with untreated Mo inducing stronger M1 polarization compared to its pre-treated counterpart. RNA transcriptional analysis identified *Mmp9* as a critical gene involved in this process, a finding confirmed through experiments with MMP9 inhibitors. These results underscore the role of *Mmp9* in mediating Mo-induced polarization and suggest that pre-treatment of Mo can mitigate the adverse effects of its early degradation on macrophages and the surrounding immune environment.

Our findings not only deepen the understanding of how Mo affects macrophage polarization but also pave the way for further exploration of its immunomodulatory properties and potential therapeutic applications, particularly through precise control of Mo degradation and regulation of critical gene expression.

## CRedit authorship contribution statement

**Danyang Liu:** Writing – original draft, Project administration, Investigation, Formal analysis, Data curation. **Jiahao Chen:** Writing – original draft, Investigation, Formal analysis, Data curation. **Jiannan Zhou:** Methodology, Investigation, Funding acquisition. **Jingtao Dai:** Software, Project administration, Methodology. **Haotian Qin:** Writing – original draft, Investigation, Funding acquisition, Formal analysis. **Guojiang Wan:** Resources, Project administration, Methodology. **Junyu Qian:** Writing – review & editing, Formal analysis, Data curation, Conceptualization. **Ping Li:** Writing – review & editing, Supervision, Project administration, Conceptualization. **Jiang Li:** Writing – original draft, Project administration, Data curation, Conceptualization.

## Declaration of competing interest

The authors declare that they have no known competing financial interests or personal relationships that could have appeared to influence the work reported in this paper.

## Acknowledgments

This research was supported by the National Natural Science Foundation of China (Grant No. 82301134), Guangdong Basic and Applied Basic Research Foundation (grant numbers 2021A1515111140, 2022A1515111092, and 2022A1515110379), Scientific Research Project of Traditional Chinese Medicine Bureau of Guangdong Province (grant number 20221267).

## Appendix A. Supplementary data

Supplementary data to this article can be found online at <https://doi.org/10.1016/j.mtbio.2025.101519>.

[org/10.1016/j.mtbio.2025.101519](https://doi.org/10.1016/j.mtbio.2025.101519).

## Data availability

The authors do not have permission to share data.

## References

- [1] D. Xia, F. Yang, Y. Zheng, Y. Liu, Y. Zhou, Research status of biodegradable metals designed for oral and maxillofacial applications: a review, *Bioact. Mater* 6 (11) (2021) 4186–4208.
- [2] B. Jia, H. Yang, Z. Zhang, X. Qu, X. Jia, Q. Wu, Y. Han, Y. Zheng, K. Dai, Biodegradable Zn–Sr alloy for bone regeneration in rat femoral condyle defect model: *in vitro* and *in vivo* studies, *Bioact. Mater.* 6 (6) (2021) 1588–1604.
- [3] W. Zhou, Y. Zheng, M. Leeftang, J. Zhou, Mechanical property, biocorrosion and *in vitro* biocompatibility evaluations of Mg–Li–(Al)–(RE) alloys for future cardiovascular stent application, *Acta Biomater.* 9 (10) (2013) 8488–8498.
- [4] Y. Chen, Z. Xu, C. Smith, J. Sankar, Recent advances on the development of magnesium alloys for biodegradable implants, *Acta Biomater.* 10 (11) (2014) 4561–4573.
- [5] J. Qian, W. Zhang, Y. Chen, P. Zeng, J. Wang, C. Zhou, H. Zeng, H. Sang, N. Huang, H. Zhang, Osteogenic and angiogenic bioactive collagen entrapped calcium/zinc phosphates coating on biodegradable Zn for orthopedic implant applications, *Biomater. Adv* 136 (2022) 212792.
- [6] Y. Qin, P. Wen, H. Guo, D. Xia, Y. Zheng, L. Jauer, R. Poprawe, M. Voshage, J. H. Schleifenbaum, Additive manufacturing of biodegradable metals: current research status and future perspectives, *Acta Biomater.* 98 (2019) 3–22.
- [7] L. Gu, R. Huang, N. Ni, P. Gu, X. Fan, Advances and prospects in materials for craniofacial bone reconstruction, *ACS Biomater. Sci. Eng.* 9 (8) (2023) 4462–4496.
- [8] Y. Lu, A. Liu, S. Jin, J. Dai, Y. Yu, P. Wen, Y. Zheng, D. Xia, Additively manufactured biodegradable Zn-based porous scaffolds to suppress osteosarcoma and promote osteogenesis, *Adv. Mater.* (2024) e2410589.
- [9] M. Mehdizade, A.R. Eivani, F. Tabatabaei, S.H. Mousavi Anijdan, H.R. Jafarian, Enhanced *in-vitro* biodegradation, bioactivity, and mechanical properties of Mg-based biocomposite via addition of calcium-silicate-based bioceramic through friction stir processing as resorbable temporary bone implant, *J. Mater. Res. Technol.* 26 (2023) 4007–4023.
- [10] C. Li, C. Guo, V. Fitzpatrick, A. Ibrahim, M.J. Zwierstra, P. Hanna, A. Lechtig, A. Nazarian, S.J. Lin, D.L. Kaplan, Design of biodegradable, implantable devices towards clinical translation, *Nat. Rev. Mater.* 5 (1) (2020) 61–81.
- [11] C. Redlich, P. Quadbeck, M. Thieme, B. Kieback, Molybdenum – a biodegradable implant material for structural applications? *Acta Biomater.* 104 (2020) 241–251.
- [12] H. Xing, P. Hu, C. He, X. Zhang, J. Han, F. Yang, R. Bai, W. Zhang, K. Wang, A. A. Volinsky, Design of high-performance molybdenum alloys via doping metal oxide and carbide strengthening: a review, *J. Mater. Sci. Technol.* 160 (2023) 161–180.
- [13] A. Toschka, G. Pöhle, P. Quadbeck, C.V. Suschek, A. Strauß, C. Redlich, M. Rana, Molybdenum as a potential biocompatible and resorbable material for osteosynthesis in craniomaxillofacial surgery—an *in vitro* study, *Int. J. Mol. Sci.* 23 (24) (2022) 15710.
- [14] M.-E. Prieto Jarabo, C. Redlich, A. Schauer, P.K.N. Alves, C. Guder, G. Poehle, T. Weissgaerber, V. Adams, U. Kappert, A. El-Armouche, A. Linke, M. Wagner, Bioreabsorbable molybdenum temporary epicardial pacing wires, *Acta Biomater.* 178 (2024) 330–339.
- [15] X. Huang, H. Hou, B. Yu, J. Bai, Y. Guan, L. Wang, K. Chen, X. Wang, P. Sun, Y. Deng, S. Liu, X. Cai, Y. Wang, J. Peng, X. Sheng, W. Xiong, L. Yin, Fully biodegradable and long-term operational primary zinc batteries as power sources for electronic medicine, *ACS Nano* 17 (6) (2023) 5727–5739.
- [16] M.H. Shin, S.M. Baek, A.V. Polyakov, I.P. Semenova, R.Z. Valiev, W.-b. Hwang, S. K. Hahn, H.S. Kim, Molybdenum disulfide surface modification of ultrafine-grained titanium for enhanced cellular growth and antibacterial effect, *Sci. Rep.* 8 (1) (2018) 9907.
- [17] S. Chen, A. Saeed, Q. Liu, Q. Jiang, H. Xu, G.G. Xiao, L. Rao, Y. Duo, Macrophages in immunoregulation and therapeutics, *Signal Transduct Target Ther* 8 (1) (2023) 207.
- [18] J. Li, X. Jiang, H. Li, M. Gelinsky, Z. Gu, Tailoring materials for modulation of macrophage fate, *Adv. Mater.* 33 (12) (2021) 2004172.
- [19] J.A. Oliveira, R. de Oliveira Alves, I.M. Nascimento, M.A.R. Hidalgo, R.M. Scarel-Caminaga, S. Cristina Pigossi, Pro- and anti-inflammatory cytokines and osteoclastogenesis-related factors in peri-implant diseases: systematic review and meta-analysis, *BMC Oral Health* 23 (1) (2023) 420.
- [20] D.-W. Zhao, C.-M. Du, K.-Q. Zuo, Y.-X. Zhao, X.-Q. Xu, Y.-B. Li, S. Tian, H.-R. Yang, Y.-P. Lu, L. Cheng, G.-Y. Xiao, Calcium–zinc phosphate chemical conversion coating facilitates the osteointegration of biodegradable zinc alloy implants by orchestrating macrophage phenotype, *Adv. Healthc. Mater* 12 (9) (2023) 2202537.
- [21] P. Li, J. Dai, Y. Li, D. Alexander, J. Capek, J. Geis-Gerstorfer, G. Wan, J. Han, Z. Yu, A. Li, Zinc based biodegradable metals for bone repair and regeneration: bioactivity and molecular mechanisms, *Mater. Today Bio* 25 (2024) 100932.
- [22] H. Yang, B. Jia, Z. Zhang, X. Qu, G. Li, W. Lin, D. Zhu, K. Dai, Y. Zheng, Alloying design of biodegradable zinc as promising bone implants for load-bearing applications, *Nat. Commun.* 11 (1) (2020) 401.
- [23] D.M. Ramos, R. Dhandapani, A. Subramanian, S. Sethuraman, S.G. Kumbar, Clinical complications of biodegradable screws for ligament injuries, *Mater. Sci. Eng. C* 109 (2020) 110423.



- [24] M. Noronha Oliveira, W.V.H. Schunemann, M.T. Mathew, B. Henriques, R. S. Magini, W. Teughels, J.C.M. Souza, Can degradation products released from dental implants affect peri-implant tissues? *J. Periodontol. Res.* 53 (1) (2018) 1–11.
- [25] L. Jin, C. Chen, Y. Li, F. Yuan, R. Gong, J. Wu, H. Zhang, B. Kang, G. Yuan, H. Zeng, T. Chen, A biodegradable Mg-based alloy inhibited the inflammatory response of THP-1 cell-derived macrophages through the TRPM7-PI3K-AKT1 signaling Axis, *Front. Immunol.* 10 (2019) 2798.
- [26] S. Terpilowska, D. Siwicka-Gieroba, A.K. Siwicki, Cytotoxicity of iron (III), molybdenum (III), and their mixtures in BALB/3T3 and HepG2 cells, *J Vet Res* 62 (4) (2018) 527–533.
- [27] K. Božinović, D. Nestić, U.G. Centa, A. Ambriović-Ristov, A. Dekanić, L. de Bisschop, M. Remškar, D. Majhen, In-vitro toxicity of molybdenum trioxide nanoparticles on human keratinocytes, *Toxicology* 444 (2020) 152564.
- [28] A. Toschka, H. Möllmann, D. Hoppe, G. Poehle, L. van Meenen, M. Seidl, N. Karnatz, M. Rana, How does the biocompatibility of molybdenum compare to the gold standard titanium? — An in vivo rat model, *Appl. Sci.* 13 (10) (2023) 6312.
- [29] H. Cao, M. Zhang, B. Xia, J. Xiong, Y. Zong, G. Hu, C. Zhang, Effects of molybdenum or/and cadmium on mRNA expression levels of inflammatory cytokines and HSPs in duck spleens, *Biol. Trace Elem. Res.* 170 (1) (2016) 237–244.
- [30] S.S. Jakobsen, G. Danscher, M. Stoltenberg, A. Larsen, J.M. Bruun, T. Mygind, K. Kemp, K. Soballe, Cobalt-chromium-molybdenum alloy causes metal accumulation and metallothionein up-regulation in rat liver and kidney, *Basic Clin. Pharmacol. Toxicol.* 101 (6) (2007) 441–446.
- [31] M. Sikora-Jasinska, L.M. Morath, M.P. Kwesiga, M.E. Plank, A.L. Nelson, A. A. Oliver, M.L. Bocks, R.J. Guillory, J. Goldman, In-vivo evaluation of molybdenum as bioabsorbable stent candidate, *Bioact. Mater* 14 (2022) 262–271.
- [32] H. Lin, Z. Song, A. Bianco, How macrophages respond to two-dimensional materials: a critical overview focusing on toxicity, *J. Environ. Sci. Health. B* 56 (4) (2021) 333–356.
- [33] J. Mayers, B. Hofman, I. Sobiech, M.P. Kwesiga, Insights into the biocompatibility of biodegradable metallic molybdenum for cardiovascular applications—a critical review, *Front. Bioeng. Biotechnol.* 12 (2024) 1457553.
- [34] M. Pettersson, P. Kelk, G.N. Belibasakis, D. Bylund, M. Molin Thorén, A. Johansson, Titanium ions form particles that activate and execute interleukin-1 $\beta$  release from lipopolysaccharide-primed macrophages, *J. Periodontol. Res.* 52 (1) (2017) 21–32.
- [35] F. Gao, E. Su, J. Hou, J. Wang, Y. Zhou, H. Qin, Z. Xie, J. Mao, H. Li, W. Tao, Y. Chen, J. Qian, G. Wan, Progressively advantageous long-term corrosion profile of Mo over Mg, Zn, and Fe from the perspective of biodegradable metals, *Corros. Sci.* 240 (2024) 112439.
- [36] L. Yin, H. Cheng, S. Mao, R. Haasch, Y. Liu, X. Xie, S.-W. Hwang, H. Jain, S.-K. Kang, Y. Su, R. Li, Y. Huang, J.A. Rogers, Dissolvable metals for transient electronics, *Adv. Funct. Mater.* 24 (5) (2014) 645–658.
- [37] L. De Rosa, C.R. Tomachuk, J. Springer, D.B. Mitton, S. Saiello, F. Bellucci, The wet corrosion of molybdenum thin film — Part I: behavior at 25°C, *MATER CORROS* 55 (8) (2004) 602–609.
- [38] Y. Shen, Y. Cheng, Y. Zheng, Insight into the biodegradation behavior of pure molybdenum under simulated inflammatory condition, *Corros. Sci.* 228 (2024) 111816.
- [39] P. Li, W. Zhang, J. Dai, A.B. Xepapadeas, E. Schweizer, D. Alexander, L. Scheideler, C. Zhou, H. Zhang, G. Wan, J. Geis-Gerstorfer, Investigation of zinc-copper alloys as potential materials for craniomaxillofacial osteosynthesis implants, *Mater. Sci. Eng. C* 103 (2019) 109826.
- [40] I.O.f. Standardization, ISO 10993-23:2021 Biological Evaluation of Medical Devices - Part 23: Tests for Irritation, ISO, Geneva, Switzerland, 2021.
- [41] C. Lorenz, J.G. Brunner, P. Kollmannberger, L. Jaafar, B. Fabry, S. Virtanen, Effect of surface pre-treatments on biocompatibility of magnesium, *Acta Biomater.* 5 (7) (2009) 2783–2789.
- [42] R. Amberg, A. Elad, D. Rothamel, T. Fienitz, G. Szakacs, S. Heilmann, F. Witte, Design of a migration assay for human gingival fibroblasts on biodegradable magnesium surfaces, *Acta Biomater.* 79 (2018) 158–167.
- [43] Y. Chen, W. Zhang, M.F. Maitz, M. Chen, H. Zhang, J. Mao, Y. Zhao, N. Huang, G. Wan, Comparative corrosion behavior of Zn with Fe and Mg in the course of immersion degradation in phosphate buffered saline, *Corros. Sci.* 111 (2016) 541–555.
- [44] A. International, Standard Guide for Laboratory Immersion Corrosion Testing of Metals, 2021, p. 10.
- [45] A. International, Standard Practice for Preparing, Cleaning, and Evaluating Corrosion Test Specimens, 2017, p. 9.
- [46] I. Iso, 10993-5: 2009 Biological Evaluation of Medical Devices—Part 5: Tests for In Vitro Cytotoxicity, International Organization for Standardization, Geneva, 2009.
- [47] R. Murali, P. Thanikaivelan, Bionic, porous, functionalized hybrid scaffolds with vascular endothelial growth factor promote rapid wound healing in Wistar albino rats, *RSC Adv.* 6 (23) (2016) 19252–19264.
- [48] J. Chen, J. Dai, J. Qian, W. Li, R. Li, D. Pang, G. Wan, P. Li, S. Xu, Influence of surface roughness on biodegradability and cytocompatibility of high-purity magnesium, *Materials* 15 (11) (2022).
- [49] P. Li, C. Schille, E. Schweizer, E. Kimmerle-Müller, F. Rupp, A. Heiss, C. Legner, U. E. Klotz, J. Geis-Gerstorfer, L. Scheideler, Selection of extraction medium influences cytotoxicity of zinc and its alloys, *Acta Biomater.* 98 (2019) 235–245.
- [50] M.D. Abrámov, P.J. Magalhães, S.J. Ram, Image processing with ImageJ, *Biophotonics Int* 11 (7) (2004) 36–42.
- [51] J. Zhou, J.L. Pathak, L. Wu, B. Chen, T. Cao, W. Wei, X. Wu, G. Chen, N. Watanabe, X. Li, J. Li, Downregulated GPX4 in salivary gland epithelial cells contributes to salivary secretion dysfunction in Sjogren's syndrome via lipid ROS/pSTAT4/AQP5 axis, *Free Radic. Biol. Med.* 218 (2024) 1–15.
- [52] M.Y. Zhang, C. Huo, J.Y. Liu, Z.E. Shi, W.D. Zhang, J.J. Qu, Y.L. Yue, Y.Q. Qu, Identification of a five autophagy subtype-related gene expression pattern for improving the prognosis of lung adenocarcinoma, *Front. Cell Dev. Biol.* 9 (2021).
- [53] D. Szklarczyk, A.L. Gable, K.C. Nastou, D. Lyon, R. Kirsch, S. Pyysalo, N. T. Doncheva, M. Legeay, T. Fang, P. Bork, L.J. Jensen, C. von Mering, The STRING database in 2021: customizable protein–protein networks, and functional characterization of user-uploaded gene/measurement sets, *Nucleic Acids Res.* 49 (D1) (2020) D605–D612.
- [54] J. Zhou, J.L. Pathak, T. Cao, B. Chen, W. Wei, S. Hu, T. Mao, X. Wu, N. Watanabe, X. Li, J. Li, CD4 T cell-secreted IFN- $\gamma$  in Sjögren's syndrome induces salivary gland epithelial cell ferroptosis, *Biochim. Biophys. Acta, Mol. Basis Dis.* 1870 (4) (2024) 167121.
- [55] L. Salwinski, D. Eisenberg, The MiSink plugin: Cytoscape as a graphical interface to the database of interacting proteins, *Bioinformatics* 23 (16) (2007) 2193–2195.
- [56] X. Li, D. Ma, X. Zha, D. Quan, D. Pan, M. Sun, B. Hu, B. Zhao, Ilomastat, a synthetic inhibitor of MMPs, prevents lung injury induced by  $\gamma$ -ray irradiation in mice, *Oncotarget* 8 (37) (2017) 60789–60808.
- [57] H. He, W. Yang, N. Su, C. Zhang, J. Dai, F. Han, M. Singhal, W. Bai, X. Zhu, J. Zhu, Z. Liu, W. Xia, X. Liu, C. Zhang, K. Jiang, W. Huang, D. Chen, Z. Wang, X. He, F. Kirchoff, Z. Li, C. Liu, J. Huan, X. Wang, W. Wei, J. Wang, H.G. Augustin, J. Hu, Activating NO-sGC crosstalk in the mouse vascular niche promotes vascular integrity and mitigates acute lung injury, *J. Exp. Med.* 220 (2) (2023).
- [58] L.L. Bennink, Y. Li, B. Kim, I.J. Shin, B.H. San, M. Zangari, D. Yoon, S.M. Yu, Visualizing collagen proteolysis by peptide hybridization: from 3D cell culture to in vivo imaging, *Biomaterials* 183 (2018) 67–76.
- [59] Z. Mardina, J. Venezuela, M.S. Dargusch, Z. Shi, A. Atrens, The influence of the protein bovine serum albumin (BSA) on the corrosion of Mg, Zn, and Fe in Zahrain's simulated interstitial fluid, *Corros. Sci.* 199 (2022) 110160.
- [60] Y. Xu, Y. Xu, W. Zhang, M. Li, H.-P. Wendel, J. Geis-Gerstorfer, P. Li, G. Wan, S. Xu, T. Hu, Biodegradable Zn-Cu-Fe alloy as a promising material for craniomaxillofacial implants: an in vitro investigation into degradation behavior, cytotoxicity, and hemocompatibility, *Front. Chem.* 10 (2022) 860040.
- [61] M.A. Maruf, M. Noor-A-Alam, W. Haider, I. Shabib, Enhancing controlled and uniform degradation of Fe by incorporating Mg and Zn aimed for bio-degradable material applications, *Mater. Chem. Phys.* 285 (2022) 126171.
- [62] D. Bian, Z. Tong, G. Gong, H. Huang, L. Fang, H. Yang, W. Gu, H. Yu, Y. Zheng, Additive manufacturing of biodegradable molybdenum—from powder to vascular stent, *Adv. Mater.* (2024) 2401614.
- [63] I.A. de Castro, R.S. Datta, J.Z. Ou, A. Castellanos-Gomez, S. Sriram, T. Daeneke, K. Kalantar-zadeh, Molybdenum oxides – from fundamentals to functionality, *Adv. Mater.* 29 (40) (2017) 1701619.
- [64] X.-T. He, X. Li, M. Zhang, B.-M. Tian, L.-J. Sun, C.-S. Bi, D.-K. Deng, H. Zhou, H.-L. Qu, C. Wu, Role of molybdenum in material immunomodulation and periodontal wound healing: targeting immunometabolism and mitochondrial function for macrophage modulation, *Biomaterials* 283 (2022) 121439.
- [65] A. Scheurle, E. Kunisch, A. Boccacini, T. Walker, T. Renkawitz, F. Westhauser, Boric acid and Molybdenum trioxide synergistically stimulate osteogenic differentiation of human bone marrow-derived mesenchymal stromal cells, *J. Trace Elem. Med. Biol.* 83 (2024) 127405.
- [66] M. Moll, A. Scheurle, Q. Nawaz, T. Walker, E. Kunisch, T. Renkawitz, A. Boccacini, F. Westhauser, Osteogenic and angiogenic potential of molybdenum-containing mesoporous bioactive glass nanoparticles: an ionic approach to bone tissue engineering, *J. Trace Elem. Med. Biol.* 86 (2024) 127518.
- [67] I. Kopova, J. Stráský, P. Harcuba, M. Landa, M. Janeček, L. Bačáková, Newly developed Ti-Nb-Zr-Ta-Si-Fe biomedical beta titanium alloys with increased strength and enhanced biocompatibility, *Mater. Sci. Eng. C* 60 (2016) 230–238.
- [68] Z. Tong, G. Gong, H. Huang, G. Cai, L. Fang, H. Yu, C. Li, Y. Zheng, D. Bian, In vitro corrosion and biocompatibility of additively manufactured biodegradable molybdenum, *Acta Biomater.* 191 (2025) 66–79.
- [69] Y. He, H. Tao, Y. Zhang, Y. Jiang, S. Zhang, C. Zhao, J. Li, B. Zhang, Y. Song, X. Zhang, Biocompatibility of bio-Mg-Zn alloy within bone with heart, liver, kidney and spleen, *Chin. Sci. Bull.* 54 (2009) 484–491.
- [70] S. Tardito, G. Martinelli, S. Soldano, S. Paolino, G. Pacini, M. Patane, E. Alessandri, V. Smith, M. Cutolo, Macrophage M1/M2 polarization and rheumatoid arthritis: a systematic review, *Autoimmun. Rev.* 18 (11) (2019) 102397.
- [71] A. Schauer, C. Redlich, J. Scheibler, G. Poehle, B. Barthel, A. Maennel, V. Adams, T. Weissgaerber, A. Linke, P. Quadbeck, Biocompatibility and degradation behavior of molybdenum in an in vivo rat model, *Materials* 14 (24) (2021) 7776.
- [72] J. Yang, Y. Zhu, D. Duan, P. Wang, Y. Xin, L. Bai, Y. Liu, Y. Xu, Enhanced activity of macrophage M1/M2 phenotypes in periodontitis, *Arch. Oral Biol.* 96 (2018) 234–242.
- [73] H. Zhang, D. Cai, X. Bai, Macrophages regulate the progression of osteoarthritis, *Osteoarthr. Cartil* 28 (5) (2020) 555–561.
- [74] A. Hozumi, Y. Nishimura, T. Nishiuma, Y. Kotani, M. Yokoyama, Induction of MMP-9 in normal human bronchial epithelial cells by TNF- $\alpha$  via NF- $\kappa$ B-mediated pathway, *Am. J. Physiol. Lung Cell Mol. Physiol.* 281 (6) (2001) L1444–L1452.
- [75] K.-C. Liang, C.-W. Lee, W.-N. Lin, C.-C. Lin, C.-B. Wu, S.-F. Luo, C.-M. Yang, Interleukin-1 $\beta$  induces MMP-9 expression via p42/p44 MAPK, p38 MAPK, JNK, and nuclear factor- $\kappa$ B signaling pathways in human tracheal smooth muscle cells, *J. Cell. Physiol.* 211 (3) (2007) 759–770.
- [76] J.-s. Chen, Q. Wang, X.-h. Fu, X.-H. Huang, X.-l. Chen, L.-q. Cao, L.-z. Chen, H.-x. Tan, W. Li, J. Bi, L.-j. Zhang, Involvement of PI3K/PTEEN/AKT/mTOR pathway in invasion and metastasis in hepatocellular carcinoma: association with MMP-9, *Hepatol. Res.* 39 (2) (2009) 177–186.

- [77] L. Yang, Q. Fu, L. Yang, Y. Zhang, HIF-1 $\alpha$ /MMP-9 promotes spinal cord central sensitization in rats with bone cancer pain, *Eur. J. Pharmacol.* 954 (2023) 175858.
- [78] D.P. Mason, R.D. Kenagy, D. Hasenstab, D.F. Bowen-Pope, R.A. Seifert, S. Coats, S. M. Hawkins, A.W. Clowes, Matrix metalloproteinase-9 overexpression enhances vascular smooth muscle cell migration and alters remodeling in the injured rat carotid artery, *Circ. Res.* 85 (12) (1999) 1179–1185.
- [79] S. Zhu, Y. Yu, Y. Ren, L. Xu, H. Wang, X. Ling, L. Jin, Y. Hu, H. Zhang, C. Miao, The emerging roles of neutrophil extracellular traps in wound healing, *Cell Death Dis.* 12 (11) (2021) 984.
- [80] Y. Della Rocca, L. Fonticoli, T.S. Rajan, O. Trubiani, S. Caputi, F. Diomede, J. Pizzicannella, G.D. Marconi, Hypoxia: molecular pathophysiological mechanisms in human diseases, *J. Physiol. Biochem.* 78 (4) (2022) 739–752.
- [81] H. Kaur, M.P. Bansal, Studies on scavenger receptors under experimental hypercholesterolemia: modulation on selenium supplementation, *Biol. Trace Elem. Res.* 143 (1) (2011) 310–319.
- [82] X. Wang, P. An, Z. Gu, Y. Luo, J. Luo, Mitochondrial metal ion transport in cell metabolism and disease, *Int. J. Mol. Sci.* 22 (14) (2021).
- [83] B. Yu, C. Cheng, Y. Wu, L. Guo, D. Kong, Z. Zhang, Y. Wang, E. Zheng, Y. Liu, Y. He, Interactions of ferritin with scavenger receptor class A members, *J. Biol. Chem.* 295 (46) (2020) 15727–15741.
- [84] A.R. Ghiasvand, S. Shadabi, E. Mohagheghzadeh, P. Hashemi, Homogeneous liquid-liquid extraction method for the selective separation and preconcentration of ultra trace molybdenum, *Talanta* 66 (4) (2005) 912–916.
- [85] W.R. Hagen, Cellular uptake of molybdenum and tungsten, *Coord. Chem. Rev.* 255 (9) (2011) 1117–1128.